

## Article

# What Is the Threshold Elevation at Which Climatic Factors Determine Snow Cover Variability? A Case Study of the Keriya River Basin

Wei Yan <sup>1,2</sup> , Yifan Wang <sup>1,2,\*</sup> , Xiaofei Ma <sup>3</sup> , Yaogeng Tan <sup>4</sup>, Junhui Yan <sup>1,2</sup>, Minghua Liu <sup>1,2</sup> and Sutao Liu <sup>1,2</sup>

<sup>1</sup> School of Geographic Sciences, Xinyang Normal University, Xinyang 464000, China; yanwei.jw@xynu.edu.cn (W.Y.); yanjh2015@126.com (J.Y.); lmhhqs@126.com (M.L.); liusutao2021@163.com (S.L.)

<sup>2</sup> Xinyang Key Laboratory of Climate Change and Environmental Evolution, Xinyang Normal University, Xinyang 464000, China

<sup>3</sup> State Key Laboratory of Desert and Oasis Ecology, Xinjiang Institute of Ecology and Geography, Chinese Academy of Sciences, Urumqi 830011, China; mxmf@ms.xjb.ac.cn

<sup>4</sup> Information Center (Hydrology Monitor and Forecast Center), Ministry of Water Resources, Beijing 100053, China; yaogengtan@mwr.gov.cn

\* Correspondence: wangyf@xynu.edu.cn

**Abstract:** Climate and topography are pivotal factors influencing snow cover variation, highlighting the significance of investigating the altitudinal response of snow cover to climate change. This study adopted a new MODIS snow cover extent product over China, reanalysis climate data, and digital elevation model (DEM) data to analyze the variation characteristics of snow cover frequency (SCF) and climatic factors with elevation in the Keriya River Basin (KRB) during the hydrological years from 2000 to 2020. The Partial Least Squares Regression (PLSR) method was utilized to explore the elevation-based relationships between SCF and climatic factors. Our findings can be summarized as follows: (1) The SCF exhibited an “increasing–decreasing–increasing–decreasing” pattern intra-annually, with insignificant monthly inter-annual variations. Only November, January, April, and May demonstrated upward trends, whereas October and December remained relatively stable, and other months exhibited declines. (2) Vertical variations in SCF and climatic factors revealed fluctuating upward trends in SCF and wind speed. On the other hand, the air temperature consistently decreased at a lapse rate ranging from 0.60 to 0.85 °C/100 m. Precipitation demonstrated “rising–falling” or “rapidly rising–slowly rising” patterns, bounded by 3821 m (range 3474–4576 m). (3) A new decision scheme, which took into account the alteration of the primary SCF controlling factors and shifts between positive and negative impacts caused by these factors, was used to determine five threshold elevation zones: 2585 m (range 2426–2723 m), 3447 m (range 3125–3774 m), 4251 m (range 4126–4375 m), 5256 m (range 4975–5524 m), and 5992 m (range 5874–6425 m). These threshold elevation zones were evident in spring, with four of these appearing in autumn (excluding 4251 m) and summer (excluding 2585 m). Only two threshold elevation zones were observed in winter with elevation values of 3447 m and 5992 m, respectively. Our findings are crucial for a deeper understanding of snow cover variation patterns at different elevations and offer essential insights for the responsible management of regional water resources.

**Keywords:** climatic factors; Keriya River Basin; partial least squares regression; snow cover; threshold elevation; trend tests



**Citation:** Yan, W.; Wang, Y.; Ma, X.; Tan, Y.; Yan, J.; Liu, M.; Liu, S. What Is the Threshold Elevation at Which Climatic Factors Determine Snow Cover Variability? A Case Study of the Keriya River Basin. *Remote Sens.* **2023**, *15*, 4725. <https://doi.org/10.3390/rs15194725>

Academic Editors: Roberto Salzano, Rosamaria Salvatori and Angelika Humbert

Received: 18 August 2023

Revised: 19 September 2023

Accepted: 25 September 2023

Published: 27 September 2023



**Copyright:** © 2023 by the authors. Licensee MDPI, Basel, Switzerland. This article is an open access article distributed under the terms and conditions of the Creative Commons Attribution (CC BY) license (<https://creativecommons.org/licenses/by/4.0/>).

## 1. Introduction

As a critical component of the cryosphere, snow cover has a significant influence on surface energy and radiation balances, hydrological cycles, atmospheric circulation, and regional socioeconomic factors [1–3]. Characterized by its high albedo, latent heat of phase transition,

and low heat conduction, snow cover significantly affects global and regional climate dynamics within the cryosphere [4–7]. Moreover, snow cover demonstrates remarkable susceptibility to climate change, a phenomenon particularly pronounced in the arid areas of Northwest China, which are characterized by fragile ecosystems [8,9]. In this context, snow resources in Northwest China have substantial climatic, environmental, hydrological, and ecological effects, which serve as vital underpinnings for sustaining the economic development of the oasis and ecosystem stability in arid areas [10,11]. Therefore, a comprehensive examination of snow cover variations within the arid areas of Northwest China is important for the effective management of water resources and environmental preservation.

Snow cover, a responsive indicator of cryospheric environmental fluctuations, exhibits pronounced susceptibility to external factors, including regional climate and topographical conditions [12–14]. Therefore, clarification of the climatic mechanisms impinging upon snow cover is of utmost significance for an in-depth understanding of the patterns of snow cover variations. Previous studies have suggested that the correlation between snow cover and climate is intricately related to elevation. For example, Shi et al. [15] investigated the response of snow cover to climate change in the source region of the Yangtze River from 2000 to 2019. Their findings clarified temperature and precipitation as primary factors affecting snow cover day (SCD), noting that the relationship between climatic parameters (temperature and precipitation) and SCD decreased significantly with increasing elevation. Li et al. [16] examined the effects of temperature and precipitation on SCF in the Altai Mountains of Xinjiang during 2001–2020 and emphasized that temperature could be the main factor affecting the SCF, with a gradual decrease in the influence as the elevation increased. Furthermore, certain studies have indicated that the primary controlling factors of snow cover may undergo alterations with increasing elevation. For instance, Hammond et al. [17] analyzed the global relationship between snow cover and climate from 2001 to 2016 and observed a heightened correlation between snow persistence and temperature at lower elevations, whereas precipitation was a more substantial factor at higher elevations. Yan et al. [18] investigated the impact of climate on snow cover in the Yurungkax River Basin during 2000–2013. They found that in the low mountain areas, air temperature was the primary factor influencing spring and summer snow cover, while winter snow cover was more responsive to precipitation. In the high mountain areas, air temperature had a greater impact on summer snow cover, while snow cover variations in spring and winter were primarily driven by precipitation. Gao et al. [19], focusing on the response of snow cover to climate change in the eastern Tibetan Plateau between 1978 and 2005, argued that temperature predominantly governed snow cover at lower elevations, with precipitation steering dynamics at high elevations. The impact of climate on snow cover exhibits elevation-dependent changes, which may be attributed to variations in climatic factors. Affected by the lapse rate, air temperature gradually decreases as elevation increases, which is further complicated by temperature inversion phenomena within mountainous areas [20–23]. Notably, prior investigations have elucidated evident vertical gradients in precipitation alterations, with a conspicuous maximum precipitation zone [24,25]. Similarly, wind speed also displays gradient characteristics with earlier research highlighting more significant wind speed fluctuations in elevated regions than in lower-altitude zones [26,27].

Currently, numerous researchers have addressed the threshold elevation of snow cover responses to climate change [28–33]. These studies contribute to a deeper understanding of the mechanisms of snow cover change at different elevations. Bi et al. [30] have proposed a threshold elevation of  $3650 \pm 150$  m in the upper Heihe River Basin. This elevation signifies a more substantial impact of temperature and precipitation on snow cover below and above this threshold, respectively. Additionally, it indicates positive and negative transformations in the effects of temperature and precipitation on snow cover. Wu et al. [29] identified two distinct threshold elevations in the Manas River Basin within the Central Tianshan Mountains. Bounded by a threshold elevation of  $3900 \pm 400$  m, snow cover exhibits an inverse correlation with temperature and a positive correlation with precipitation below this elevation and vice versa above it. Below the threshold elevation of  $1400 \pm 100$  m,

precipitation emerges as the primary controlling factor for snow cover, whereas above this elevation, temperature becomes the principal factor. However, current research has predominantly examined snow cover threshold elevation under the singular influences of temperature and precipitation, ignoring the threshold elevation influenced by multiple climatic factors. Previous studies have demonstrated that wind speed has a significant impact on snow cover [34–36]. Therefore, this study endeavored to explore the threshold elevation of snow cover under the combined impacts of air temperature, precipitation, and wind speed.

As a representative inland river basin, snow cover is one of the main sources of runoff supply in the Keriya River Basin (KRB). The annual average snow cover percentage accounts for 34.09% of the entire basin area, with a maximum ratio of 45.02% [37]. In addition, the remote location of the basin and limited anthropogenic influence position it as a natural research area for investigating the response of snow cover to climate change. Currently, certain scholars have delineated the annual and seasonal variability of snow cover in the KRB and analyzed the influence of climatic factors on a pixel scale [37,38]. However, the issue of the threshold elevation remains unexplored. Therefore, the objectives of this study were as follows: (1) to elucidate the monthly variation patterns of snow cover within the KRB throughout the 2001–2020 hydrological years, (2) to analyze the vertical distribution characteristics of snow cover and associated climatic factors, and (3) to discuss the threshold elevation of snow cover response to climatic factors.

## 2. Materials and Methods

### 2.1. Study Area

Regulated by the Keriya Hydrological Station (36°45′N, 81°48′E), the KRB is located in the northern margin of the Tibetan Plateau and the eastern section of the West Kunlun Mountains, spanning coordinates of 35°11′–36°27′N and 81°27′–82°50′E (Figure 1a). The terrain in the KRB is intricate and marked by rugged contours, characterized by lower elevations in the northern region and higher elevations in the south. The area of the KRB measures 8350.25 km<sup>2</sup>, where the area exceeding 4000 m above sea level constitutes 86.7% (Figure 1b). High-altitude zones predominantly harbor glaciers, occupying 8.2% of the entire area [39], thereby significantly impacting the ecological environment and socioeconomic structure of the basin. The KRB lies within the domain of a typical warm temperate arid desert climate, characterized by an annual average air temperature of −7.3 °C and average annual precipitation and runoff depth of 431.9 mm and 91.3 mm, respectively. In particular, approximately 80% of the annual precipitation and runoff are concentrated between May to September [37].

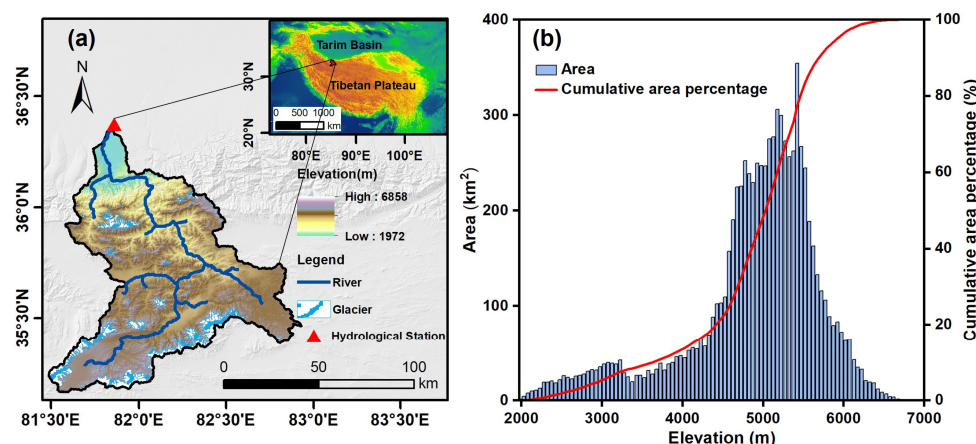


**Figure 1.** Geographical overview of the KRB (a) and area distribution of the area within different elevation zones (b). Note: The KRB is divided into elevation zones at 50 m intervals. The area of each elevation zone is calculated based on the digital elevation model (DEM) data from the Shuttle Radar Topography Mission (SRTM).

## 2.2. Data Sources

The data employed in this study mainly included snow cover, climatic parameters (air temperature, precipitation, and wind speed), and DEM, as shown in Table 1. A specialized MODIS day-by-day cloud-free snow cover dataset, denoted as a new MODIS snow cover extent product over China, was primarily adopted to extract snow cover information for the study area. The spatial resolution was 500 m with a high accuracy of 93% [40,41]. Reanalysis climate datasets can effectively address the limitations of sparse distribution and limited availability of meteorological station data in the KRB. By conducting a comparative analysis with meteorological and hydrological station data, we discovered that the 1-km monthly mean temperature dataset for China [42–46], ERA5-Land precipitation data [47], and HAR v2 wind speed data [48] have high applicability in this study area. The correlation coefficients were above 0.97 (for air temperature), 0.64 (for precipitation), and reached 0.50 (for wind speed), respectively [37]. These datasets were used to explore the impact of climate on snow cover. Additionally, SRTM DEM data were selected to analyze the topographical features of the KRB.

**Table 1.** Data utilized in this study.

Name	Spatial Resolution	Temporal Resolution	Period	Resource	Website
Snow cover	500 m × 500 m	Daily	2000–2020	A new MODIS snow cover extent product over China	<a href="http://data.tpdc.ac.cn/">http://data.tpdc.ac.cn/</a> (accessed on 1 October 2022)
Air temperature	1 km × 1 km	Monthly	2000–2020	1-km monthly mean temperature dataset for China	<a href="http://data.tpdc.ac.cn/">http://data.tpdc.ac.cn/</a> (accessed on 5 January 2023)
Precipitation	0.1° × 0.1°	Monthly	2000–2020	ERA5-Land	<a href="https://cds.climate.copernicus.eu/">https://cds.climate.copernicus.eu/</a> (accessed on 5 January 2023)
Wind speed	10 km × 10 km	Monthly	2000–2020	HAR v2	<a href="https://www.klima.tu-berlin.de/">https://www.klima.tu-berlin.de/</a> (accessed on 8 January 2023)
DEM	90 m	N/A	2000	SRTM	<a href="http://srtm.csi.cgiar.org">http://srtm.csi.cgiar.org</a> (accessed on 1 October 2022)

Note: N/A indicates data with no temporal resolution.

To maintain consistency in spatial resolution across snow cover data, reanalysis climate datasets, and DEM data, a statistical downscaling method was employed to resample reanalysis climate datasets to 500 m, while a bilinear interpolation method was utilized to resample DEM data to the same resolution. In view of the hydrological characteristics of the KRB, the interval spanning 1 September to 31 August of the subsequent year was designated as a hydrological year (HY). The snow cover data and reanalysis climate datasets were extracted using the HY scale.

## 2.3. Methods

### 2.3.1. Snow Cover Frequency (SCF)

The SCF, representing the ratio of days exhibiting snow cover on a given pixel to the total number of days within the examined timeframe, was used to analyze the snow cover variation in the KRB:

$$SCF = \frac{D_s}{D} \times 100\% \quad (1)$$

where  $D_s$  and  $D$  represent the number of days with snow cover for a specific pixel and the total number of days within a particular time period (month or season), respectively.

### 2.3.2. Sen's Slope and Mann–Kendall Trend Test Methods

The investigation into the monthly variation patterns of SCF in the KRB involved a combination of the Sen's slope and Mann–Kendall trend test methods [49–52]. Sen's slope was applied to determine the magnitude of the variation trend, while the Mann–Kendall trend test provided insights into the statistical significance of the trend. In the context of a time series denoted as  $x_1, x_2, \dots, x_n$ , where  $n$  represents the length of the time sequence, Sen's slope ( $Q$ ) is defined as follows:

$$Q = \text{Median}\left(\frac{x_j - x_i}{j - i}\right) \quad (2)$$

The statistic ( $S$ ) is defined as:

$$S = \sum_{i=1}^{n-1} \sum_{j=i+1}^n \text{sgn}(x_j - x_i) \quad (3)$$

where  $x_j$  and  $x_i$  represent the observed values corresponding to years  $j$  and  $i$ , respectively,  $j > i$ , and the symbolic function  $\text{sgn}$  is defined as follows:

$$\text{sgn}(\theta) = \begin{cases} 1 & \theta > 0 \\ 0 & \theta = 0 \\ -1 & \theta < 0 \end{cases} \quad (4)$$

The variance of  $S$  is calculated as follows:

$$\text{var}(S) = \left[ n(n-1)(2n+5) - \sum_{p=1}^q t_p(t_p-1)(2t_p+5) \right] / 18 \quad (5)$$

where  $t_p$  denotes the number of data points in group  $p$  and  $q$  represents the total number of tied groups.

Finally, the standardized statistic  $Z_c$  is obtained. The formula is as follows:

$$Z_c = \begin{cases} \frac{S-1}{\sqrt{\text{var}(S)}} & S > 0 \\ 0 & S = 0 \\ \frac{S+1}{\sqrt{\text{var}(S)}} & S < 0 \end{cases} \quad (6)$$

At a 95% confidence level, when  $|Z_c| > 1.96$ , a significant trend can be observed within the time series. A  $Z_c$  value exceeding 1.96 suggests a considerable increase in the sequence's variations, whereas a  $Z_c$  value below  $-1.96$  implies a substantial decline in the time series.

### 2.3.3. Partial Least Squares Regression (PLSR)

The PLSR method can effectively eliminate multiple correlations among multiple independent variables, which combines three analysis methods: Principal Component Analysis (PCA), Canonical Correlation Analysis (CCA), and Multiple Linear Regression (MLR) [53,54]. In this study, the PLSR method with a single dependent variable was employed to analyze the degree of influence of different climatic factors on the SCF. Firstly, the input data were standardized using the Z-score method. Subsequently, the required components were sequentially extracted from the independent variables for regression analysis. Finally, the regression equation of the standardized dependent variable  $\hat{y}^*$  on the standardized independent variables  $x_1^*, \dots, x_p^*$  was obtained as follows:

$$\hat{y}^* = \alpha_1 x_1^* + \alpha_2 x_2^* + \dots + \alpha_p x_p^* \quad (7)$$

where  $\alpha_p$  represents the regression coefficient of  $x_p^*$ .

The primary SCF controlling factors in each elevation zone within the KRB were determined by comparing the absolute values of the PLSR coefficients of air temperature, precipitation, and wind speed. The procedure of the PLSR methodology is shown in Figure 2.

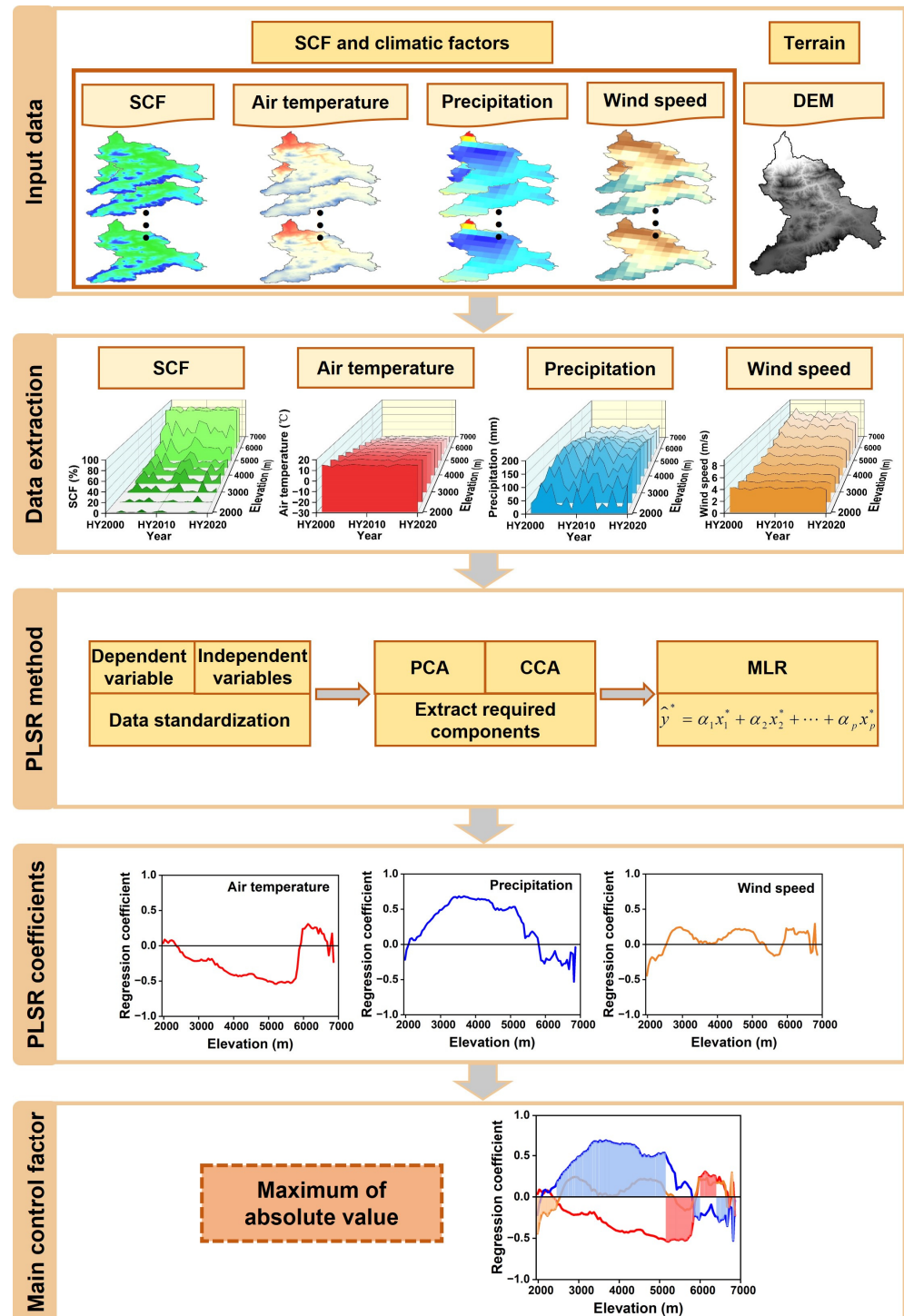
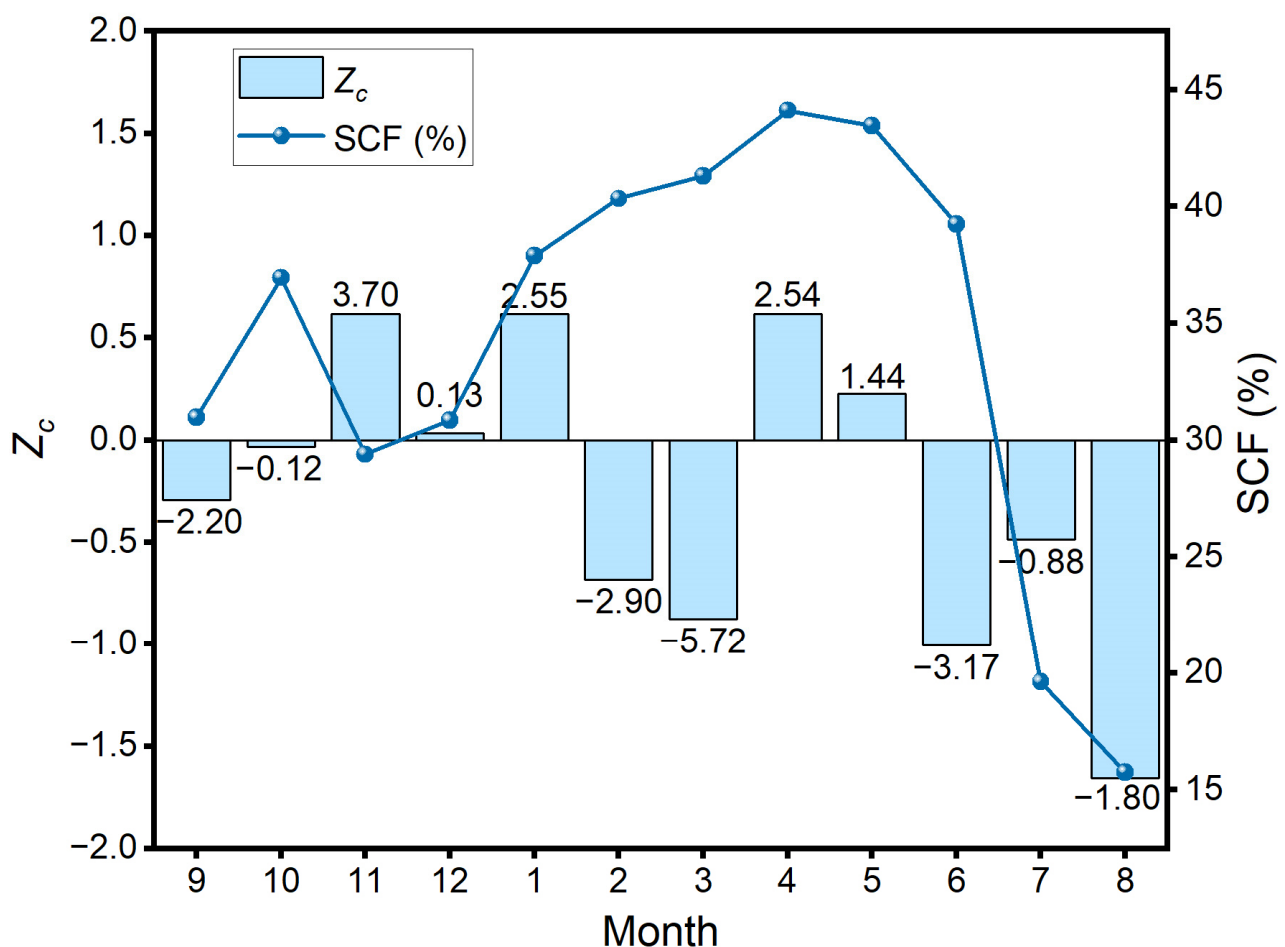


Figure 2. Schematic diagram of the process using the PLSR method. In the “Data extraction” section, we only presented the extraction results for a subset of elevation zones. In this study, elevation zones were actually extracted at 50 m intervals.

### 3. Results

#### 3.1. Variation Characteristics of Snow Cover

The intra-annual and inter-annual variation patterns of the monthly SCF in the KRB were analyzed (Figure 3). From the perspective of intra-annual variation, the dynamic variation in monthly SCF in the KRB across a hydrological year was divided into four distinct stages, illustrating a discernible trend of “increasing–decreasing–increasing–decreasing” with the boundaries of October, November, and April. The increase in monthly SCF commenced in September, reaching its initial peak (36.96%) in October, followed by a slight decline to its first trough (29.39%) in November. Subsequently, from November to April of the following year, monthly SCF exhibited consistent and rapid growth at a rate of 2.95%/month, reaching its maximum value (44.12%) in April. However, due to increasing air temperatures, the SCF decreased rapidly from April to August, demonstrating an average decline rate of  $-7.63\%$  per month at a significance level of 0.05 and reaching its lowest point (15.76%) for the entire hydrological year in August. In terms of inter-annual variation, November, January, April, and May demonstrated insubstantial upward trends, with November registering the largest increase trend at 3.70%/decade. In contrast, the monthly SCF within October and December exhibited relative stability in inter-annual trends, with marginal shifts of  $-0.12\%$ /decade and  $0.13\%$ /decade, respectively, closely approximating zero. The remaining months exhibited a downward trend, characterized by decline rates ranging from  $-5.72\%$ /decade to  $-0.88\%$ /decade. Only the SCF variation in August reached a significance level of 0.1.



**Figure 3.** Intra-annual and inter-annual variation characteristics of monthly SCF in the KRB during 2001–2020. The number value at the top of each bar denotes the variation rate of monthly SCF with a unit of %/decade.

### 3.2. Vertical Distribution Characteristics of Snow Cover and Climatic Factors

In this study, the elevation zones were divided into intervals of 50 m. Subsequently, the vertical distribution of snow cover and climatic factors was derived at seasonal and monthly scales by extracting the average values of SCF, air temperature, precipitation, and wind speed for each elevation zone (Figure 4). In particular, with the elevation of 4653 m (range 4576–4825 m) and 5949 m (range 5824–6073 m) as the boundary, the SCF exhibited a trend of “gradual increase–rapid increase–being stable” as the elevation increased (Figure 4(a1–a4)). Below an elevation of 4653 m (range 4576–4825 m), the SCF exhibited gradual growth with increasing elevation during autumn, spring, and summer, while winter witnessed a “decreasing–increasing–decreasing” pattern. Spanning the range of 4653 m (range 4576–4825 m) to 5949 m (range 5824–6073 m), the SCF displayed a rapid increase. Beyond the threshold elevation of 5949 m (range 5824–6073 m), the SCF tended to remain stable during winter and slightly decreased during autumn, spring, and summer, with the most pronounced decrease observed during summer.

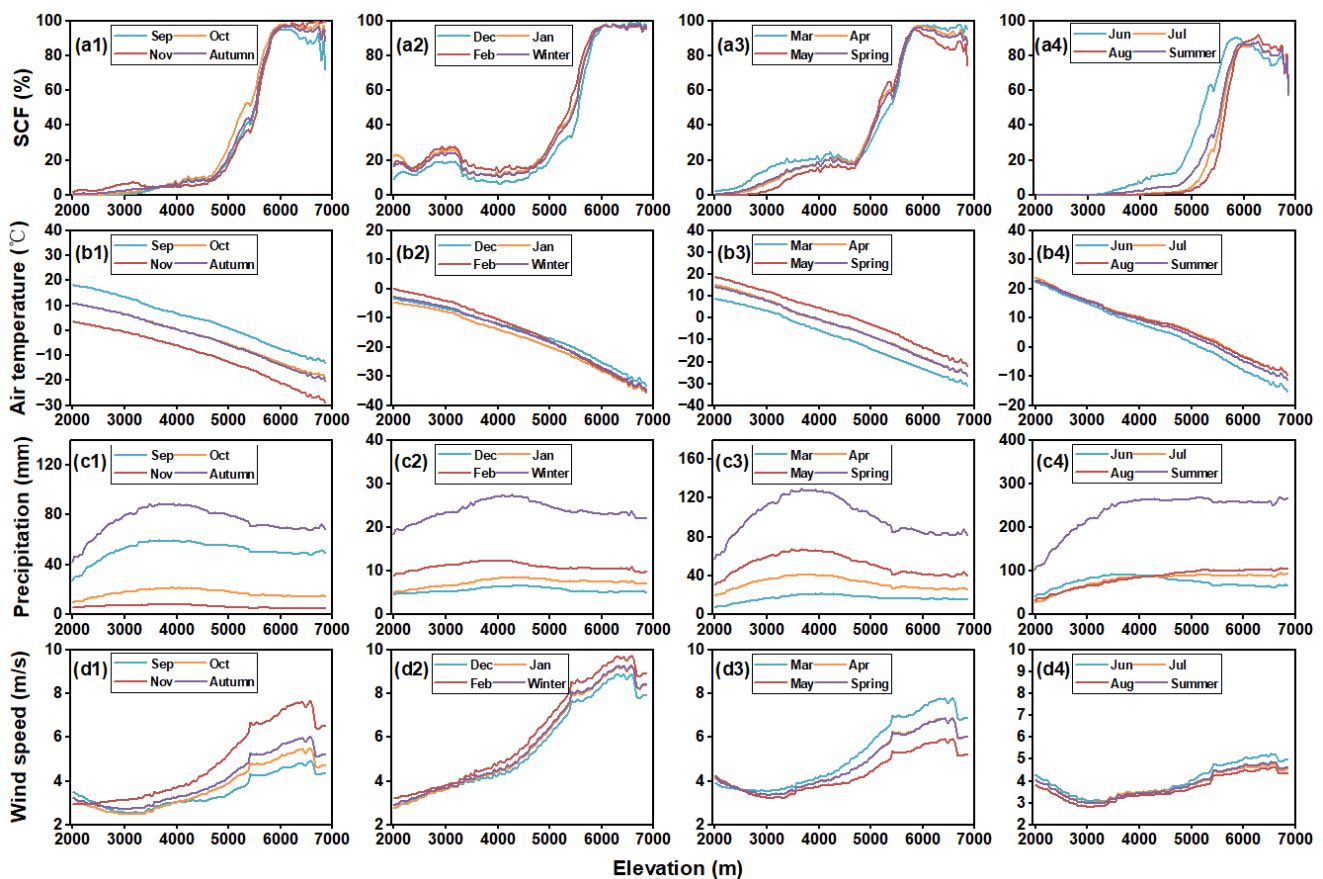


**Figure 4.** Variations in seasonal and monthly SCF (a1–a4), air temperature (b1–b4), precipitation (c1–c4), and wind speed (d1–d4) across different elevations.

There was an evident negative correlation between air temperature and elevation at both seasonal and monthly scales (Figure 4(b1–b4)). We further calculated the air temperature lapse rate for each month, which identified an intra-annual variation with a unimodal trend (Figure 5a). Specifically, the air temperature lapse rate exhibited relatively high values during spring, with the highest rate observed in April ( $0.85\text{ }^{\circ}\text{C}/100\text{ m}$ ) and the lowest recorded in December ( $0.60\text{ }^{\circ}\text{C}/100\text{ m}$ ). This phenomenon could be attributed to the influence of springtime snowmelt, which leads to an increase in bare land in lower elevation areas, triggering higher air temperatures. However, a substantial presence of perennial snow and glaciers remained in the elevated regions, contributing to consistently low air temperatures and consequently inducing a considerable temperature difference

between low and high elevations. Sun et al. [55] reported that the lapse rate of the average temperature on the northern slopes of the Kunlun Mountains peaked during spring, which was consistent with the findings presented in this study.

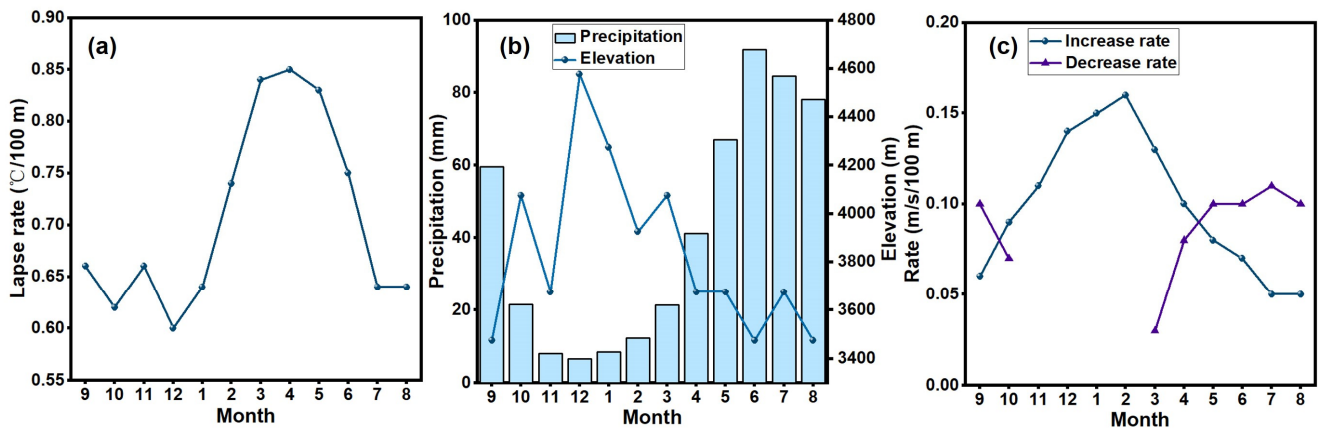


**Figure 5.** Intra-annual variations in (a) air temperature lapse rate, (b) the maximum precipitation zone and the corresponding precipitation (except July and August), and (c) the change rate of wind speed with elevation.

Precipitation patterns indicated distinct trends, with a threshold elevation of 3821 m (range 3474–4576 m) (Figure 4(c1–c4)). Below this elevation, precipitation increased rapidly across all seasons and months. Conversely, above this elevation, precipitation experienced a gradual increase during July, August, and the summer season, while it gradually decreased during the remaining seasons and months. In this study, the threshold elevation and its corresponding precipitation of each month were calculated, which denoted the maximum precipitation zone, with the exception of July and August (Figure 5b). Remarkably, December showcased the highest threshold elevation (4576 m) coupled with a precipitation value of 6.7 mm, whereas September, June, and August had the lowest threshold elevation (3474 m) with precipitation values of 59.6 mm, 92.0 mm, and 78.1 mm, respectively. In terms of intra-annual variations, the threshold elevation was the highest during winter and reached the nadir during summer, whereas precipitation trends demonstrated an inverse pattern. Notably, the maximal precipitation zone within the Yarkant River Basin is situated at approximately 5520 m, which exceeds the results derived in this study [56]. This difference could be attributed to prior research determining the maximal precipitation zone using the glacier equilibrium line, whereas the present study established this zone based on ERA5-Land precipitation data.

At both seasonal and monthly scales, wind speed demonstrated a characteristic trajectory marked by “gradual decrease/increase–rapid increase–rapid decrease”, delineated by elevation thresholds of 3061 m (range 3025–3322 m) and 6566 m (range 6529–6575 m) (Figure 4(d1–d4)). Below 3061 m (range 3025–3322 m), the wind speed witnessed a gradual increase during November and the corresponding winter months, while exhibiting a continuous decline during other seasons and months. Wind speed exhibited a constant and incremental increase from 3061 m (range 3025–3322 m) to 6566 m (range 6529–6575 m), followed by a notable and rapid decrease above an elevation of 6566 m (range 6529–6575 m). Based on the relationship between wind speed and elevation, this study determined the increase rate of wind speed for each month from November to February, along with the decrease rate below 3061 m (range 3025–3322 m) and an increase rate above 3061 m (range 3025–3322 m) for other months (Figure 5c). The increase rate reached its peak in February at 0.16 m/s/100 m, while the maximum decrease rate was identified in July at 0.11 m/s/100 m. Winter demonstrated the highest increase rate in wind speed, followed by spring, autumn, and ultimately summer, which was consistent with the ranking observed in average wind speed trends.

### 3.3. Vertical Distribution Characteristics of the Main Control Factors of SCF

The relationship between the SCF and climatic factors was analyzed by applying the PLSR method. Subsequently, the regression coefficients of the air temperature, precipitation, and wind speed for each elevation zone were derived. By comparing the maximum absolute values of these regression coefficients, we obtained the variations in the main SCF controlling factors with elevation (Figure 6).

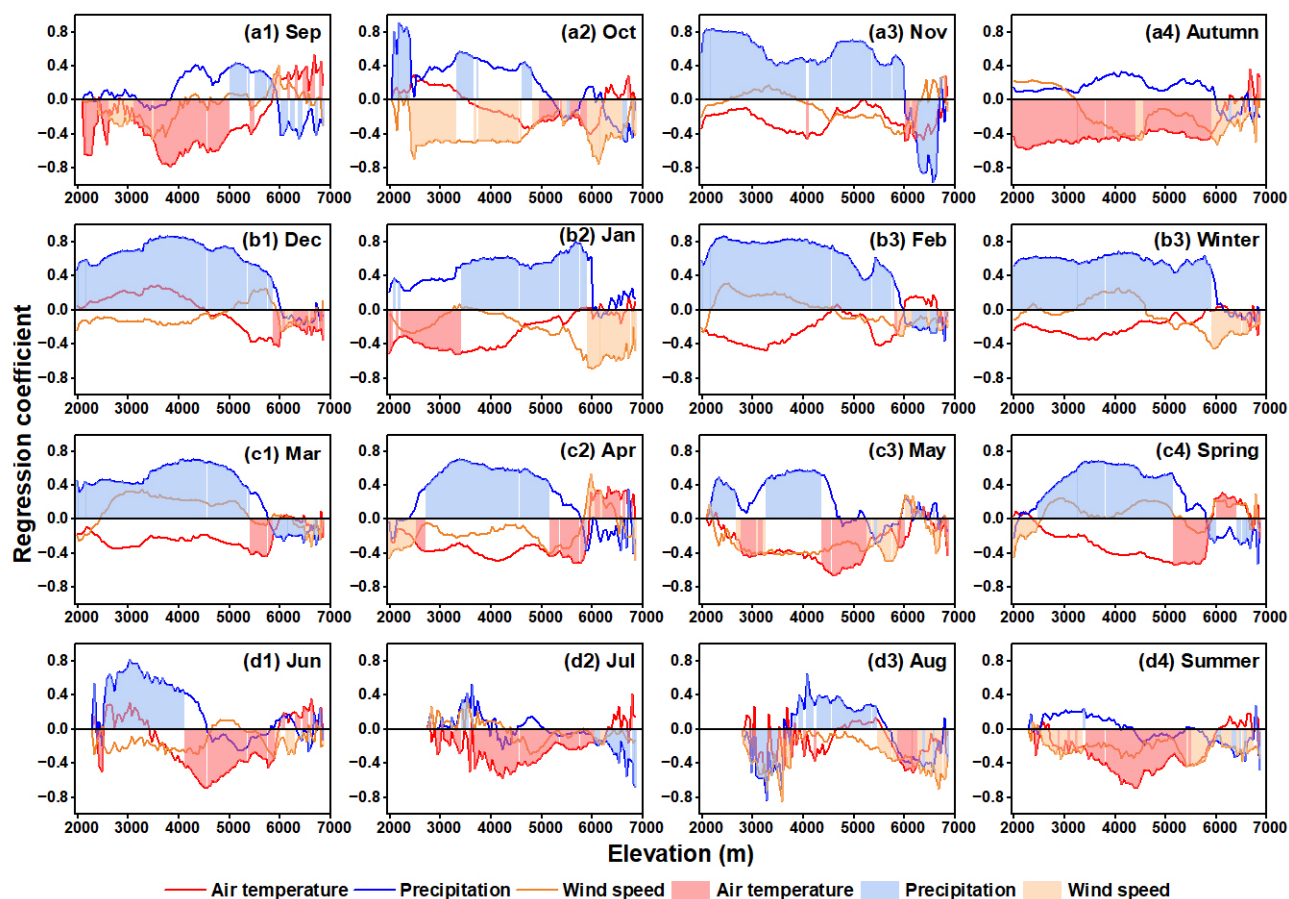


**Figure 6.** Variations in the main controlling factors of SCF with elevation in different seasons and months. The curves in red, blue, and orange represent the regression coefficients of SCF influenced by air temperature, precipitation, and wind speed, respectively. The color-filled sections highlight the main controlling factors across elevation zones.

The autumnal SCF was delimited by an elevation of 5924 m, which was primarily controlled by the adverse impacts of air temperature and wind speed, accounting for 90.40% and 9.34%, respectively (Figure 6(a4)). During September, SCF below 2626 m and within the 3125–5025 m was mainly affected by the adverse influences of air temperature, while within the elevation range of 2626–3125 m, the SCF was primarily attributed to the negative impact of wind speed. Within the range of 5025–6025 m, SCF was beneficially affected by precipitation. However, elevations exceeding 6025 m indicated alternating dynamics, where the SCF was alternately controlled by air temperature (positive influence) coupled with precipitation (negative influence) (Figure 6(a1)). In October, the SCF exhibited dominant effects of air temperature, precipitation, and wind speed, accounting for 39.73%, 17.50%, and 42.70%, respectively. Furthermore, air temperature affected the SCF between the ranges of 4975–5924 m, while the SCF beneath 2426 m and between 3322 m and 3774 m was beneficially influenced by precipitation. The SCF spanning from 2426–3322 m, 3774–4975 m, and above 5924 m was mainly controlled by the adverse influences of wind speed (Figure 6(a2)). Precipitation played a pivotal role in affecting the SCF for November,

with its impact transitioning from positive to negative at the critical threshold elevation of 6025 m (Figure 6(a3)).

Below 5924 m, the winter SCF was primarily affected by precipitation with an average influence degree of 0.59. Nevertheless, above this elevation, the winter SCF was predominantly controlled by wind speed, albeit with a less significant average influence degree of  $-0.30$  (Figure 6(b4)). Additionally, the threshold elevation in December was at 5874 m. Below this threshold, the SCF was substantially affected by precipitation, exhibiting an average influence degree of 0.68. Above this threshold, the influence oscillated between the adverse impacts of air temperature and wind speed (Figure 6(b1)). In January, the main SCF controlling factors displayed distinct patterns across the different elevation ranges. Below 3430 m, between 3430 m and 5924 m, and above 5924 m, the SCF was primarily controlled by the impacts of air temperature (negative), precipitation (positive), and wind speed (negative), constituting proportions of 8.15%, 85.99%, and 5.86%, respectively (Figure 6(b2)). Throughout February, the SCF was mainly controlled by the impact of precipitation. With increasing elevation, its influence degree initially increased, followed by a fluctuant decrease, eventually turning negative upon reaching an elevation of 6025 m (Figure 6(b3)).

In spring, air temperature and precipitation emerged as the principal controlling factors for the SCF, accounting for 40.17% and 58.35%, respectively. The influence of air temperature on the SCF was concentrated within the elevation range of 5175–6425 m, with a transition from negative to positive impact at 5924 m. On the other hand, precipitation served as the main controlling factor at elevations of 2475–5175 m and above 6425 m. Only the SCF below 2475 m was adversely affected by wind speed, accounting for 1.48% (Figure 6(c4)). In March, within the elevation range of 5423–5874 m, the SCF was primarily controlled by the air temperature, accounting for 19.88%. Conversely, below 5423 m and above 5874 m, the SCF was mainly affected by precipitation, accounting for 79.93% (Figure 6(c1)). In April, below 2723 m and within the elevation range of 2723–5175 m, the SCF was primarily determined by the negative effect of wind speed and the positive impact of precipitation, with influence degrees of  $-0.35$  and 0.58, respectively. Moreover, above 5175 m, the dominant controlling factor shifted to air temperature, transitioning from a negative to a positive impact at an elevation of 5973 m (Figure 6(c2)). In May, air temperature, precipitation, and wind speed acted as the primary SCF controlling factors, contributing proportions of 52.19%, 17.66%, and 29.98%, respectively. Within these influences, the SCF within the elevation ranges of 2675–3273 m and 4375–5275 m was predominantly affected by the adverse impacts of air temperature. The SCF below 2675 m and within the 3273–4375 m range was beneficially affected by precipitation. Moreover, the SCF within the elevation range of 5275–5874 m was primarily determined by the negative effects of wind speed. The SCF exceeding 5874 m experienced combined effects of air temperature and wind speed, albeit with relatively minor consequences (Figure 6(c3)).

In summer, the SCF exhibited pronounced sensitivity to air temperature and wind speed, contributing dominant negative effects, accounting for 70.00% and 26.62%, respectively. Within the elevation range of 3430–5524 m, air temperature primarily controlled the SCF, whereas wind speed emerged as the predominant factor below 3430 m and above 5524 m (Figure 6(d4)). In June, the SCF below 4126 m was positively affected by precipitation, accounting for 12.94%, while the SCF was negatively affected by air temperature within the range of 4126–5924 m, constituting 79.70%. Above 5924 m, it was jointly regulated by air temperature, precipitation, and wind speed (Figure 6(d1)). In July, the SCF demonstrated elevation-constrained behavior delineated by a threshold of 6073 m. Below this threshold, the SCF was predominantly affected by air temperature, accounting for 90.61%. Above this threshold, the predominant influence shifted to precipitation, constituting 2.43% (Figure 6(d2)). In August, the SCF was primarily controlled by precipitation below an elevation of 5474 m. Notably, the impact of precipitation on the SCF shifted from positive to negative at an elevation of 3774 m. Wind speed became the major influencing factor of SCF within the 5474–5874 m range and above 6273 m, while within the eleva-

tion range of 5874–6273 m, the SCF was primarily attributed to the adverse impact of air temperature (Figure 6(d3)).

#### 4. Discussion

##### 4.1. Compared with the Threshold Elevation of Previous Studies

In this study, we developed a new decision scheme to determine the threshold elevation by concurrently assessing alterations in the primary SCF controlling factors and transitions in positive and negative impacts. Based on the recurrent distribution characteristics of the threshold elevations determined for four seasons and each month, we delineated the threshold elevation zones and calculated the average and range values (by maximum and minimum) for each elevation zone (Figure 7). There exist five distinct threshold elevation zones in the KRB, situated at elevations of 2585 m (range 2426–2723 m), 3447 m (range 3125–3774 m), 4251 m (range 4126–4375 m), 5256 m (range 4975–5524 m), and 5992 m (range 5874–6425 m), respectively. The lowest threshold elevation zone was determined to be 2585 m (range 2426–2723 m) based on the specific threshold elevations observed at 2626 m (September), 2426 m (October), 2723 m (April), 2675 m (May), and 2475 m (spring). The threshold elevation zone of 3447 m (range 3125–3774 m) was identified by combining distinct elevations, including 3125 m (September), 3322 m (October), 3774 m (October), 3430 m (January), 3273 m (May), 3774 m (August), and 3430 m (summer). Additionally, by analyzing the threshold elevations at 4375 m (May) and 4126 m (June), a threshold elevation range of 4251 m (range 4126–4375 m) was identified. The interval denoted by 5256 m (range 4975–5524 m) indicated threshold elevations of 5025 m (September), 4975 m (October), 5423 m (March), 5175 m (April), 5275 m (May), 5175 m (spring), 5474 m (August), and 5524 m (summer). Furthermore, a distinct threshold elevation zone of 5992 m (range 5874–6425 m) was established by considering the threshold elevations occurring across all seasons (excluding summer) and months. Instances of multiple threshold elevations were predominantly concentrated in the transitional seasons of spring and autumn, with notable occurrences of up to five threshold elevations occurring in October and May. This phenomenon could be attributed to the dynamic variability of climate during these transition periods, contributing to the alternating modulation of the SCF by a multitude of climatic factors.

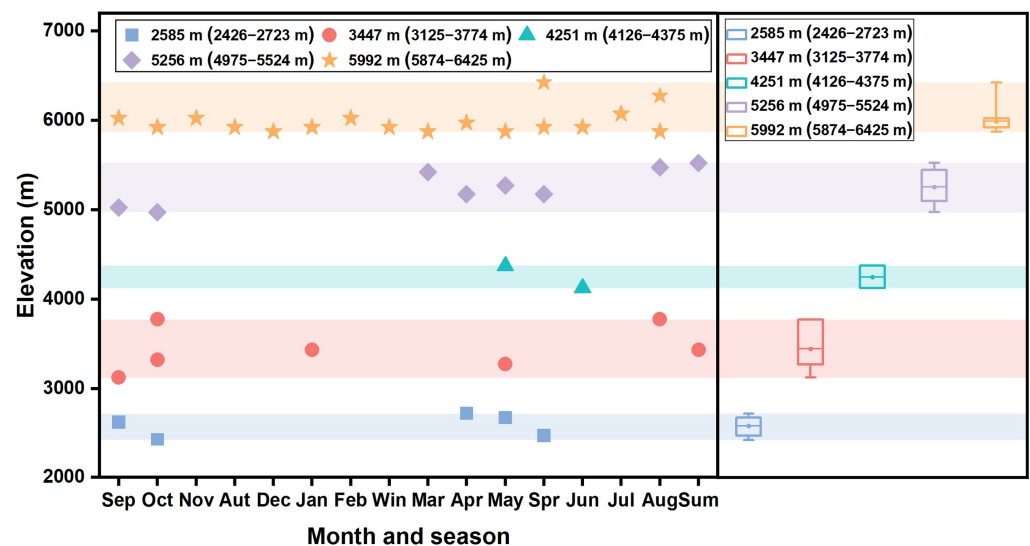


**Figure 7.** Distribution of threshold elevation in the four seasons and each month. On the right of the figure, the whiskers represent the minimum and maximum in threshold elevation zones, the boxes show the 25th percentile and 75th percentile of threshold elevation zones, and the points in the box represent the average threshold elevation.

Table 2 lists the identified threshold elevation ranges reported by previous studies. Numerous studies have successfully delineated threshold elevations within the range of 1500 m to 2000 m, though these elevations are notably lower than the study area in this study [28,29,31–33]. Certain studies have also been consistent with the results of this study, identifying threshold elevations close to 3500 m [28–30]. One of the threshold elevations identified by Ban et al. [28] was approximately 6000 m, which closely corresponds to the highest threshold elevation identified in this study. Currently, most studies have proposed the existence of a single threshold elevation range. In contrast, Wu et al. [29] and Ban et al. [28] identified two and three distinct threshold elevation zones, respectively. Compared with the threshold elevation zones delineated in this study, differences emerged not only in the quantity but also in the range of the identified threshold elevation zones, which may be caused by the following four aspects:

**Table 2.** Threshold elevations determined in different studies.

Study Area	Data	Threshold Elevation	Method	Reference
Yarlung Zangbo River basin	MOD10A2 snow cover	2100 ± 200 m	Pearson correlation	Ban et al. [28]
	MOD11A2 land surface temperature	3200 ± 300 m	The intersection point of the two correlation coefficient lines	
	CHIRPS precipitation	5925 ± 125 m		
Manas River Basin in the Central Tianshan Mountains	MOD10A2 snow cover	1400 ± 100 m	Pearson correlation	Wu et al. [29]
	MOD11A2 land surface temperature	3900 ± 400 m	The intersection point of the two correlation coefficient lines	
	CHIRPS precipitation			
Upper Heihe River Basin	MOD10A1, MYD10A1, and MOD10A2 snow cover	3650 ± 150 m	Pearson correlation	Bi et al. [30]
	Air temperature from two weather stations and MOD11A2 land surface temperature		The intersection point of the regression lines of correlation coefficients between high altitude and low altitude	
	APHRODITE precipitation			
Six mountains of the Western United States	WRF (SWE, air temperature, and precipitation)	1580–2181 m	Pearson correlation	Scalzitti et al. [31]
			The intersection point of two fitting lines with correlation coefficients	
Eastern central region of the Columbia River basin in the Central Rocky Mountains	SNOTEL (SWE, temperature, and precipitation)	1560 ± 120 m	Pearson correlation	Sospedra-Alfonso et al. [32]
			The intersection point of two least squares regression lines with correlation coefficients	
Three main mountainous areas of Switzerland	MeteoSwiss (snow depth, air temperature, and precipitation)	1400 ± 200 m	Least squares linear regressions	Morán-Tejeda et al. [33]
			The intersection point of two fitting lines with regression coefficients	
Keriya River Basin	A new MODIS snow cover extent product over China 1-km monthly mean temperature dataset for China ERA5-Land precipitation HAR v2 wind speed	2585 m (range 2426–2723 m) 3447 m (range 3125–3774 m) 4251 m (range 4126–4375 m) 5256 m (range 4975–5524 m) 5992 m (range 5874–6425 m)	Partial Least Squares Regression	This study
			Alterations in the primary SCF controlling factors and transitions in positive and negative impacts of main control factors	

Firstly, it is essential to acknowledge the discrepancies in the dataset composition. Secondly, there exist differences in the climatic factors chosen. Previous studies predominantly focused on temperature and precipitation as primary variables. However, this study

added wind speed data to comprehensively analyze the impacts of climatic factors on snow cover. Thirdly, methodological disparities between research endeavors substantially influenced the results. Most studies have employed the Pearson correlation method to establish threshold elevations by identifying the intersection of correlation coefficient lines or correlation coefficient fitting lines between climatic elements and snow cover. However, the correlations among climatic factors might affect the accuracy of results derived from the Pearson correlation method. Therefore, this study adopted the PLSR method to eliminate the interaction between climatic factors. Furthermore, we considered both the alterations of the SCF controlling factors and the transitions between positive and negative impacts of these factors to determine threshold elevations. Finally, the diverse climatic conditions across distinct geographical regions might engender disparate mechanisms by which climatic factors affect snow cover. These potentially contributed to the difference in the research results.

#### 4.2. Future Work

All the reanalysis climate data utilized in this study were validated against meteorological station data, effectively capturing authentic climatic variations within the KRB [37]. However, the reanalysis climate data, including precipitation and wind speed, featured spatial resolutions of  $0.1^\circ$  and 10 km, respectively. In the future, it might be worthwhile to consider employing data with even finer resolutions for more detailed analysis. Wu et al. [57] revealed contrasting correlations between climate elements and MODIS data within the high-elevation zones of the Tianshan Mountains compared with the correlation between climate elements and snow water equivalent data. Subsequent investigations should consider probing the disparities in the impacts of climatic elements on snow cover while employing diverse snow cover products. Additionally, this study only delineated the impacts of air temperature, precipitation, and wind speed on snow cover variations. Expanding the analysis to include additional climatic variables, such as evapotranspiration and solar radiation, holds promise for further unraveling the intricate interplay between snow cover and climatic factors.

#### 5. Conclusions

In this study, we established a connection between the SCF, climatic factors, and elevation in the KRB by integrating snow cover data, reanalysis climate data, and DEM data. The methodology employed included the utilization of the PLSR method to probe the altitudinal impacts of climatic factors on the SCF and delineate zones of threshold elevations. The results of this study can be summarized as follows: (1) Temporal variations in the monthly SCF exhibited a bimodal distribution, reaching the highest value of 44.12% in April and the lowest of 15.76% in August. On a monthly scale, inter-annual variations in the SCF tended to be largely insignificant, with more months displaying decreasing trends than exhibiting upward trends. (2) The SCF and wind speed demonstrated a fluctuating upward trend with increasing elevation. Conversely, air temperature was inversely correlated with elevation, with the air temperature lapse rate peaking in April ( $0.85^\circ\text{C}/100\text{ m}$ ) and reaching its nadir in December ( $0.60^\circ\text{C}/100\text{ m}$ ). Precipitation increased rapidly below an elevation of 3474–4576 m (average 3821 m) and displayed diverse trends above this elevation, including slow increases and rapid decreases in different months. (3) Threshold elevations were determined through a new decision scheme that integrated the changes in the main control factors of SCF and shifts in positive and negative impacts of the main control factors, and these threshold elevations are 2585 m (range 2426–2723 m), 3447 m (range 3125–3774 m), 4251 m (range 4126–4375 m), 5256 m (range 4975–5524 m), and 5992 m (range 5874–6425 m), respectively. These delineated threshold elevation zones were most pronounced during spring and the corresponding months, followed by autumn and subsequently summer, with the least occurrences observed in winter.

The new decision scheme for identifying threshold elevations in this study can be a notable reference for related studies in most regions worldwide. The results might

provide valuable insights into a more in-depth understanding of snow variation patterns, rendering significant contributions to enhance our comprehension of regional water resource sustainability.

**Author Contributions:** Conceptualization, W.Y. and Y.W.; methodology, W.Y. and X.M.; software, M.L.; validation, J.Y. and Y.T.; formal analysis, S.L.; data curation, Y.W.; writing—original draft preparation, W.Y. and Y.W.; writing—review and editing, W.Y.; supervision, X.M. All authors have read and agreed to the published version of the manuscript.

**Funding:** This research was funded by the Natural Science Foundation of Henan (232300421250, 222300420522), the Open Project of Key Laboratory, Xinjiang Uygur Autonomous Region (2023D04073), the Key Scientific Research Project in Colleges and Universities of Henan Province (22A170019), the Nanhu Scholars Program for Young Scholars of XYNU, and the Scientific Research Foundation of Graduate School of Xinyang Normal University (2022KYJJ017).

**Data Availability Statement:** Not applicable.

**Acknowledgments:** We would like to express our sincere thanks to the anonymous reviewers.

**Conflicts of Interest:** The authors declare no conflict of interest.

## References

- Déry, S.J.; Brown, R.D. Recent Northern Hemisphere snow cover extent trends and implications for the snow-albedo feedback. *Geophys. Res. Lett.* **2007**, *34*, L22504. [[CrossRef](#)]
- Chen, X.; Yang, Y.; Ma, Y.; Li, H. Distribution and attribution of terrestrial snow cover phenology changes over the Northern Hemisphere during 2001–2020. *Remote Sens.* **2021**, *13*, 1843. [[CrossRef](#)]
- Brown, R.D.; Robinson, D.A. Northern Hemisphere spring snow cover variability and change over 1922–2010 including an assessment of uncertainty. *Cryosphere* **2011**, *5*, 219–229. [[CrossRef](#)]
- Shen, Y.; Su, H.; Wang, G.; Mao, W.; Wang, S.; Han, P.; Wang, N.; Li, Z. The responses of glaciers and snow cover to climate change in Xinjiang (I): Hydrological effects. *J. Glaciol. Geocryol.* **2013**, *35*, 513–527. [[CrossRef](#)]
- Yao, T.; Qin, D.; Shen, Y.; Zhao, L.; Wang, N.; Lu, A. Cryospheric changes and their impacts on regional water cycle and ecological conditions in the Qinghai-Tibetan Plateau. *Chin. J. Nat.* **2013**, *35*, 179–186. [[CrossRef](#)]
- Sood, V.; Singh, S.; Taloor, A.K.; Prashar, S.; Kaur, R. Monitoring and mapping of snow cover variability using topographically derived NDSI model over north Indian Himalayas during the period 2008–2019. *Appl. Comput. Geosci.* **2020**, *8*, 100040. [[CrossRef](#)]
- Yan, J.; Wei, R.; Wang, J.; Niu, J.; Ji, S.; Lu, S.; Li, X. Study on spatial-temporal variations of snow cover days and its indicating climatic significance in the Middle and Lower Reaches of Yangtze River for the past 50 years. *J. Xinyang Norm. Univ. (Nat. Sci. Ed.)* **2022**, *35*, 92–96. [[CrossRef](#)]
- Dong, C. Remote sensing, hydrological modeling and in situ observations in snow cover research: A review. *J. Hydrol.* **2018**, *561*, 573–583. [[CrossRef](#)]
- Tan, X.; Wu, Z.; Mu, X.; Gao, P.; Zhao, G.; Sun, W.; Gu, C. Spatiotemporal changes in snow cover over China during 1960–2013. *Atmos. Res.* **2019**, *218*, 183–194. [[CrossRef](#)]
- Chen, Y.; Zhang, X.; Fang, G.; Li, Z.; Wang, F.; Qin, J.; Sun, F. Potential risks and challenges of climate change in the arid region of northwestern China. *Reg. Sustain.* **2020**, *1*, 20–30. [[CrossRef](#)]
- Qin, D.; Yao, T.; Ding, Y.; Ren, J. *Introduction to Cryospheric Science*; Springer Geography: Beijing, China, 2021.
- Rupp, D.E.; Mote, P.W.; Bindoff, N.L.; Stott, P.A.; Robinson, D.A. Detection and attribution of observed changes in Northern Hemisphere spring snow cover. *J. Clim.* **2013**, *26*, 6904–6914. [[CrossRef](#)]
- Qin, D.; Liu, S.; Li, P. Snow cover distribution, variability, and response to climate change in western China. *J. Clim.* **2006**, *19*, 1820–1833. [[CrossRef](#)]
- Dye, D.G.; Tucker, C.J. Seasonality and trends of snow-cover, vegetation index, and temperature in northern Eurasia. *Geophys. Res. Lett.* **2003**, *30*, 1405. [[CrossRef](#)]
- Shi, M.; Yuan, Z.; Hong, X.; Liu, S. Spatiotemporal Variation of Snow Cover and Its Response to Climate Change in the Source Region of the Yangtze River, China. *Atmosphere* **2022**, *13*, 1161. [[CrossRef](#)]
- Li, H.; Li, Z.; Chen, P.; Peng, J. Spatio-temporal variation of snow cover in Altai Mountains of Xinjiang in recent 20 years and its influencing factors. *Arid. Zone Res.* **2023**, *40*, 1040–1051. [[CrossRef](#)]
- Hammond, J.C.; Saavedra, F.A.; Kampf, S.K. Global snow zone maps and trends in snow persistence 2001–2016. *Int. J. Climatol.* **2018**, *38*, 4369–4383. [[CrossRef](#)]
- Yan, W.; Liu, J.; Luo, G.; Dong, K.; Lu, W.; Du, X. Snow cover area changes in the Yurungkax River Basin of West Kunlun Mountains during 2000–2013 using MODIS data. *Prog. Geogr.* **2014**, *33*, 315–325. [[CrossRef](#)]
- Gao, J.; Williams, M.W.; Fu, X.; Wang, G.; Gong, T. Spatiotemporal distribution of snow in eastern Tibet and the response to climate change. *Remote Sens. Environ.* **2012**, *121*, 1–9. [[CrossRef](#)]

20. Liu, M.; Ma, J.; Wang, L.; Lu, S.; Yan, J.; Liu, J.; He, Z.; Cui, Y. Spatial and temporal variations of shallow ground temperature in the Huaihe River Source and its response to recent global warming hiatus. *J. Xinyang Norm. Univ. (Nat. Sci. Ed.)* **2023**, *36*, 180–185. [[CrossRef](#)]
21. He, Y.; Wang, K. Contrast patterns and trends of lapse rates calculated from near-surface air and land surface temperatures in China from 1961 to 2014. *Sci. Bull.* **2020**, *65*, 1217–1224. [[CrossRef](#)]
22. Noad, N.C.; Bonnaventure, P.P.; Gilson, G.F.; Jiskoot, H.; Garibaldi, M.C. Surface-based temperature inversion characteristics and impact on surface air temperatures in northwestern Canada from radiosonde data between 1990 and 2016. *Arct. Sci.* **2023**, *9*, 545–563. [[CrossRef](#)]
23. Zhao, G.; Han, Y.; Liu, W.; Zhang, R.; Meng, J.; Zeng, X. Spatial-temporal variations of extreme temperature events in Xinjiang from 1961 to 2016. *J. Xinyang Norm. Univ. (Nat. Sci. Ed.)* **2021**, *34*, 248–254. [[CrossRef](#)]
24. Ménégoz, M.; Valla, E.; Jourdain, N.C.; Blanchet, J.; Beaumet, J.; Wilhelm, B.; Gallée, H.; Fettweis, X.; Morin, S.; Anquetin, S. Contrasting seasonal changes in total and intense precipitation in the European Alps from 1903 to 2010. *Hydrol. Earth Syst. Sci.* **2020**, *24*, 5355–5377. [[CrossRef](#)]
25. Luo, L.; Dan, Z.; Zhu, L.; Zhang, H. Vertical Gradient Changes of Temperature and Precipitation in the Sygera Mountains, Southeastern Qinghai-Xizang Plateau. *Plateau Meteorol.* **2021**, *40*, 37–46. [[CrossRef](#)]
26. Lin, C.; Yang, K.; Qin, J.; Fu, R. Observed coherent trends of surface and upper-air wind speed over China since 1960. *J. Clim.* **2013**, *26*, 2891–2903. [[CrossRef](#)]
27. Ge, J.; Feng, D.; You, Q.; Zhang, W.; Zhang, Y. Characteristics and causes of surface wind speed variations in Northwest China from 1979 to 2019. *Atmos. Res.* **2021**, *254*, 105527. [[CrossRef](#)]
28. Ban, C.; Xu, Z.; Zuo, D.; Liu, X.; Zhang, R.; Wang, J. Vertical influence of temperature and precipitation on snow cover variability in the Yarlung Zangbo River basin, China. *Int. J. Climatol.* **2021**, *41*, 1148–1161. [[CrossRef](#)]
29. Wu, S.; Zhang, X.; Du, J.; Zhou, X.; Tuo, Y.; Li, R.; Duan, Z. The vertical influence of temperature and precipitation on snow cover variability in the Central Tianshan Mountains, Northwest China. *Hydrol. Process.* **2019**, *33*, 1686–1697. [[CrossRef](#)]
30. Bi, Y.; Xie, H.; Huang, C.; Ke, C. Snow cover variations and controlling factors at upper Heihe River Basin, Northwestern China. *Remote Sens.* **2015**, *7*, 6741–6762. [[CrossRef](#)]
31. Scalzitti, J.; Strong, C.; Kochanski, A. Climate change impact on the roles of temperature and precipitation in western U.S. snowpack variability. *Geophys. Res. Lett.* **2016**, *43*, 5361–5369. [[CrossRef](#)]
32. Sospedra-Alfonso, R.; Melton, J.R.; Merryfield, W.J. Effects of temperature and precipitation on snowpack variability in the Central Rocky Mountains as a function of elevation. *Geophys. Res. Lett.* **2015**, *42*, 4429–4438. [[CrossRef](#)]
33. Morán-Tejeda, E.; López-Moreno, J.I.; Beniston, M. The changing roles of temperature and precipitation on snowpack variability in Switzerland as a function of altitude. *Geophys. Res. Lett.* **2013**, *40*, 2131–2136. [[CrossRef](#)]
34. Zhang, C.; Mou, N.; Niu, J.; Zhang, L.; Liu, F. Spatio-temporal variation characteristics of snow depth and snow cover days over the Tibetan Plateau. *Water* **2021**, *13*, 307. [[CrossRef](#)]
35. She, J.; Zhang, Y.; Li, X.; Feng, X. Spatial and temporal characteristics of snow cover in the Tizinafu watershed of the Western Kunlun Mountains. *Remote Sens.* **2015**, *7*, 3426–3445. [[CrossRef](#)]
36. Dharpure, J.K.; Patel, A.; Goswami, A.; Kulkarni, A.V.; Snehmani. Spatiotemporal snow cover characterization and its linkage with climate change over the Chenab river basin, western Himalayas. *GISci. Remote Sens.* **2020**, *57*, 882–906. [[CrossRef](#)]
37. Yan, W.; Wang, Y.; Ma, X.; Liu, M.; Yan, J.; Tan, Y.; Liu, S. Snow Cover and Climate Change and Their Coupling Effects on Runoff in the Keriya River Basin during 2001–2020. *Remote Sens.* **2023**, *15*, 3435. [[CrossRef](#)]
38. Ma, X.; Yan, W.; Zhao, C.; Kundzewicz, Z.W. Snow-cover area and runoff variation under climate change in the West Kunlun Mountains. *Water* **2019**, *11*, 2246. [[CrossRef](#)]
39. Liu, S.; Guo, W.; Xu, J. *The Second Glacier Inventory Dataset of China (Version 1.0) (2006–2011)*; A Big Earth Data Platform for Three Poles: Beijing, China, 2012. [[CrossRef](#)]
40. Hao, X. *A New MODIS Snow Cover Extent Product over China (2000–2020)*; National Tibetan Plateau Data Center: Lanzhou, China, 2021. [[CrossRef](#)]
41. Hao, X.; Huang, G.; Zheng, Z.; Sun, X.; Ji, W.; Zhao, H.; Wang, J.; Li, H.; Wang, X. Development and validation of a new MODIS snow-cover-extent product over China. *Hydrol. Earth Syst. Sci.* **2022**, *26*, 1937–1952. [[CrossRef](#)]
42. Peng, S. *1-Km Monthly Mean Temperature Dataset for China (1901–2021)*; National Tibetan Plateau Data Center: Lanzhou, China, 2020. [[CrossRef](#)]
43. Peng, S.; Gang, C.; Cao, Y.; Chen, Y. Assessment of climate change trends over the Loess Plateau in China from 1901 to 2100. *Int. J. Climatol.* **2018**, *38*, 2250–2264. [[CrossRef](#)]
44. Peng, S.; Ding, Y.; Wen, Z.; Chen, Y.; Cao, Y.; Ren, J. Spatiotemporal change and trend analysis of potential evapotranspiration over the Loess Plateau of China during 2011–2100. *Agric. For. Meteorol.* **2017**, *233*, 183–194. [[CrossRef](#)]
45. Ding, Y.; Peng, S. Spatiotemporal trends and attribution of drought across China from 1901–2100. *Sustainability* **2020**, *12*, 477. [[CrossRef](#)]
46. Peng, S.; Ding, Y.; Liu, W.; Li, Z. 1 km monthly temperature and precipitation dataset for China from 1901 to 2017. *Earth Syst. Sci. Data* **2019**, *11*, 1931–1946. [[CrossRef](#)]

47. Muñoz Sabater, J. ERA5-Land Monthly Data from 1950 to Present: Copernicus Climate Change Service (C3S) Climate Data Store (CDS). 2019. Available online: <https://cds.climate.copernicus.eu/cdsapp#!/dataset/reanalysis-era5-land-monthly-means?tab=overview> (accessed on 21 May 2023).
48. Wang, X.; Tolksdorf, V.; Otto, M.; Scherer, D. WRF-based dynamical downscaling of ERA5 reanalysis data for High Mountain Asia: Towards a new version of the High Asia Refined analysis. *Int. J. Climatol.* **2021**, *41*, 743–762. [[CrossRef](#)]
49. Mann, H.B. Nonparametric tests against trend. *Econometrica* **1945**, *13*, 245–259. [[CrossRef](#)]
50. Kendall, M.G. *Rank Correlation Methodss*, 4th ed.; Charles Griffin: London, UK, 1975; ISBN 0195208374.
51. Salmi, T.; Määttä, A.; Anttila, P.; Ruoho-Airola, T.; Amnell, T. Detecting trends of annual values of atmospheric pollutants by the Mann-Kendall test and Sen’s slope estimates. In *The Excel Template Application MAKESENS*; Finish Meteorological Institute: Helsinki, Finland, 2002.
52. Burgan, H.I. The short-term and seasonal trend detection of sediment discharges in Turkish rivers. *Rocz. Ochr. Sr.* **2022**, *24*, 214–230. [[CrossRef](#)]
53. Geladi, P.; Kowalski, B.R. Partial least-squares regression: A tutorial. *Anal. Chim. acta* **1986**, *185*, 1–17. [[CrossRef](#)]
54. Barker, M.; Rayens, W. Partial least squares for discrimination. *J. Chemom.* **2003**, *17*, 166–173. [[CrossRef](#)]
55. Sun, C.; Chen, W.; Shen, Y. Unraveling the distribution patterns of near-surface temperature lapse rates in the Northwestern Kunlun Mountains. *J. Mt. Sci.* **2022**, *19*, 1168–1181. [[CrossRef](#)]
56. Yang, Z. *Glacier Water Resources in China*; Gansu Science and Technology Press: Lanzhou, China, 1991.
57. Wu, S.; Zhang, X.; Du, J.; Wang, H. Evaluating the different responses to climatic factors between snow water equivalent and snow cover area in the Central Tianshan Mountains. *Theor. Appl. Climatol.* **2022**, *148*, 1563–1576. [[CrossRef](#)]

**Disclaimer/Publisher’s Note:** The statements, opinions and data contained in all publications are solely those of the individual author(s) and contributor(s) and not of MDPI and/or the editor(s). MDPI and/or the editor(s) disclaim responsibility for any injury to people or property resulting from any ideas, methods, instructions or products referred to in the content.